

An Earth-Sized Planet in a 5.4h Orbit Around a Nearby K dwarf[★]

Kaya Han Taş¹, Gudmundur Stefansson¹, Syarief N. M. Fariz¹, Esha Garg¹, Juan I. Espinoza-Retamal^{2,3,1}, Elise Koo¹, David Bruijne¹, Jacob Luhn⁴, Eric B. Ford^{5,6,7,8}, Suvrath Mahadevan^{5,6}, Sarah E. Logsdon⁹, Caleb I. Cañas¹⁰, Te Han²¹, Mark E. Everett⁹, Jaime A. Alvarado-Montes^{11,12}, Cullen Blake¹⁴, William D. Cochran²², Jiayin Dong^{15,16}, Rachel B. Fernandes^{5,6**}, Mark R. Giovinnazzi¹⁷, Samuel Halverson¹⁴, Shubham Kanodia¹⁸, Daniel Krolkowski¹⁹, Michael McElwain¹⁰, Joe Ninan²⁰, Leonardo A. Paredes¹⁹, Paul Robertson²¹, and Christian Schwab¹³

- ¹ Anton Pannekoek Institute for Astronomy, University of Amsterdam, Science Park 904, 1098 XH Amsterdam, The Netherlands
- ² Instituto de Astrofísica, Pontificia Universidad Católica de Chile, Av. Vicuña Mackenna 4860, 782-0436 Macul, Santiago, Chile
- ³ Millennium Institute for Astrophysics, Santiago, Chile
- ⁴ Jet Propulsion Laboratory, California Institute of Technology, 4800 Oak Grove Drive, Pasadena, CA 91109, USA
- ⁵ Department of Astronomy & Astrophysics, 525 Davey Laboratory, The Pennsylvania State University, University Park, PA 16802, USA
- ⁶ Center for Exoplanets and Habitable Worlds, 525 Davey Laboratory, The Pennsylvania State University, University Park, PA 16802, USA
- ⁷ Institute for Computational and Data Sciences, The Pennsylvania State University, University Park, PA 16802, USA
- ⁸ Center for Astrostatistics, 525 Davey Laboratory, The Pennsylvania State University, University Park, PA 16802, USA
- ⁹ U.S. National Science Foundation National Optical-Infrared Astronomy Research Laboratory, 950 N. Cherry Avenue, Tucson, AZ 85719, USA
- ¹⁰ NASA Goddard Space Flight Center, Greenbelt, MD 20771, USA
- ¹¹ Australian Astronomical Optics, Macquarie University, Balacalava Road, North Ryde, NSW 2109, Australia
- ¹² Astrophysics and Space Technologies Research Centre, Macquarie University, Balacalava Road, North Ryde, NSW 2109, Australia
- ¹³ School of Mathematical and Physical Sciences, Macquarie University, Balacalava Road, North Ryde, NSW 2109, Australia
- ¹⁴ Department of Physics and Astronomy, University of Pennsylvania, 209 South 33rd Street, Philadelphia, PA 19104, USA
- ¹⁵ Center for Computational Astrophysics, Flatiron Institute, 162 Fifth Avenue, New York, NY 10010, USA
- ¹⁶ Department of Astronomy, University of Illinois at Urbana-Champaign, Urbana, IL 61801, USA
- ¹⁷ Department of Physics and Astronomy, Amherst College, Amherst, MA 01002, USA
- ¹⁸ Earth and Planets Laboratory, Carnegie Institution for Science, 5241 Broad Branch Road, NW, Washington, DC 20015, USA
- ¹⁹ Steward Observatory, University of Arizona, 933 N. Cherry Ave, Tucson, AZ 85721, USA
- ²⁰ Department of Astronomy and Astrophysics, Tata Institute of Fundamental Research, Homi Bhabha Road, Colaba, Mumbai 400005, India
- ²¹ Department of Physics & Astronomy, The University of California, Irvine, Irvine, CA 92697, USA
- ²² McDonald Observatory and Center for Planetary Systems Habitability, The University of Texas at Austin, Austin, TX 78730, USA

ABSTRACT

We present the discovery and confirmation of the ultra-short period (USP) planet TOI-2431 b orbiting a nearby ($d \sim 36$ pc) late K star ($T_{\text{eff}} = 4109 \pm 28$ K) using observations from the Transiting Exoplanet Survey Satellite (TESS), precise radial velocities with the NEID and the Habitable-zone Planet Finder (HPF) spectrographs, as well as ground-based high contrast imaging from NESSI. TOI-2431 b has a period of 5 hours and 22 minutes, making it one of the shortest-period exoplanets known to date. TOI-2431 b has a radius of $1.536 \pm 0.033 R_{\oplus}$, and a mass of $6.2 \pm 1.2 M_{\oplus}$, suggesting it has a density compatible with an Earth-like composition and, due to its high irradiation, is likely a ‘lava-world’ with a $T_{\text{eq}} = 2063 \pm 30$ K. We estimate that the current orbital period is only 30% larger than the Roche-limit orbital period, and that it has an expected orbital decay timescale of only ~ 31 Myr. Finally, due to the brightness of the host star ($V = 10.9$, $K = 7.6$), TOI-2431 b has a high Emission Spectroscopy Metric of 27, making it one of the best USP systems for atmospheric phase-curve analysis.

Key words. exoplanets – ultra-short period planets

1. Introduction

Ultra-short period (USP) planets are planets that have an orbital period smaller than one day (Sahu et al. 2006; Adams et al. 2016; Goyal & Wang 2025). Of the ~ 6000 exoplanets discovered so far, about 150 are confirmed USP planets as per the NASA Exoplanet Archive¹ (Akeson et al. 2013; Christiansen et al. 2025).

¹ <https://exoplanetarchive.ipac.caltech.edu/>

[★] Based on observations obtained with the Hobby-Eberly Telescope (HET), which is a joint project of the University of Texas at Austin, the Pennsylvania State University, Ludwig-Maximilians-Universitaet Muenchen, and Georg-August Universitaet Goettingen. The HET is named in honor of its principal benefactors, William P. Hobby and Robert E. Eberly.

^{**} President’s Postdoctoral Fellow

Most USP planets have radii $< 2 R_{\oplus}$ (Winn et al. 2018). They tend to have Earth-like compositions (Dai et al. 2019), although some are consistent with compositions enhanced in iron as compared to the Earth (Price & Rogers 2020; Uzsoy et al. 2021). Due to their close-in orbits, USP planets tend to have surface temperatures in excess of 2000 K, suggesting their surfaces are likely molten.

Using data from the *Kepler* mission, Sanchis-Ojeda et al. (2014) found that the occurrence rate of USP planets is $1.1 \pm 0.4\%$ for M dwarfs, $0.51 \pm 0.07\%$ for G dwarfs, and only $0.15 \pm 0.05\%$ for F dwarfs, suggesting that the presence of a USP planet depends on the spectral type of the star. Further, Winn et al. (2018) noted that USP planets are often found in compact multi-planet systems, with high orbital period ratios, where the orbital period of the innermost USP planet and its closest neighbor typically has a ratio of four or more (Steffen & Farr 2013; Winn et al. 2018; Pu & Lai 2019). This ratio is larger than the value generally seen in multi-planet systems discovered by *Kepler* (Fabrycky et al. 2017). Further, Dai et al. (2018) showed that the dispersion of orbital inclinations among transiting planets tends to be larger when a USP planet is part of the system.

The origin of USP planets is not fully understood, and a few different formation scenarios have been proposed. One scenario is that rocky USP planets represent the exposed cores of hot Jupiters (Jackson et al. 2013; Valsecchi et al. 2015; Königl et al. 2017). However, Winn et al. (2017) found the metallicity distribution of USP-planet host stars to be different from that of hot Jupiter host stars. In addition, they found that the metallicity distributions of stars hosting rocky USP planets, and stars hosting $2 - 4 R_{\oplus}$ planets with orbital periods of a few days, are identical. From this perspective, USP planets could represent the exposed cores of such smaller ($2 - 4 R_{\oplus}$) gaseous planets and/or super-Earths (e.g., Lundkvist et al. 2016; Lee & Chiang 2017). Since USP planets are typically found in the star’s dust sublimation region, it is unlikely that they formed at their present location (Murgas et al. 2022), and therefore likely migrated to their current orbits. A number of USP migration mechanisms have been proposed, most involving tidal dissipation from different sources and initial conditions (Schlaufman et al. 2010; Lee & Chiang 2017). Petrovich et al. (2019) studied compact multi-planet systems and suggested the possibility of eccentricity excitation from secular dynamical chaos. Pu & Lai (2019) suggested that the outer planets tidally interact with each other and with the innermost planet, damping its eccentricity to close to zero and shrinking its semi-major axis in a quasi-equilibrium state. Millholland & Spalding (2020) proposed that obliquity-driven tidal migration could be a way to obtain USP orbits. Finally, Tu et al. (2025) found that the occurrence of USP planets increases with stellar age, and suggested that different tidal migration pathways may be responsible for younger and older USP planets.

Due to their close-in and short-period orbits, USP planets are some of the most favorable systems for thermal phase-curve and secondary eclipse observations. Owing to their high stellar irradiation, it is likely that any hydrogen-helium (H/He) atmosphere they may have had, has been completely stripped away (Sanchis-Ojeda et al. 2014; Lundkvist et al. 2016; Lopez 2017). Their atmospheric and surface characteristics—such as albedo, phase shifts, and temperature differences between the day-and night sides—can shed light on the primary surface mineralogy and/or the presence of a secondary atmosphere (Hu et al. 2012; Demory et al. 2016; Kreidberg et al. 2019; Whittaker et al. 2022; Zhang et al. 2024; Dai et al. 2024).

The Transiting Exoplanet Survey Satellite (TESS; Ricker et al. 2014) is enabling the detection of USP planets around

nearby bright stars, facilitating precise mass constraints with ground-based Doppler spectroscopy, and phase-curve observations with JWST. LHS 3844 b (Vanderspek et al. 2019), a rocky super-earth orbiting an M dwarf 15 pc away, was the first USP planet found by TESS, and more recent discoveries include GJ 367 b (Lam et al. 2021), TOI-6255 b (Dai et al. 2024), and TOI-6324 b (Lee et al. 2025).

In this paper, we present the discovery of TOI-2431 b, a USP planet with a period of ~ 0.224 days, making it the sixth shortest period planet known to date. TOI-2431 is a bright ($V = 10.9$ mag, $K = 7.6$ mag) K7V star at a distance of 36 pc. TOI-2431 was identified as a TESS Objects of Interest, and statistically validated by Guerrero et al. (2021). Here, we present a detailed characterization of the system, including precise RV follow-up observations to determine its mass and thereby confirming its planetary nature. Additionally, due to the short period of the planet, we show that TOI-2431 b is very close to its Roche limit, and has one of the highest Emission Spectroscopy Metrics (ESM; Kempton et al. 2018) with JWST enabling the possibility for high signal-to-noise-ratio phase-curve observations.

This paper is structured as follows. In Section 2, we describe the observations and data reduction. In Section 3, we discuss the parameters of the host star. In Section 4 we discuss the Transit and RV joint analysis, and we present our planet parameter constraints in Section 5. In Section 6, we discuss our search for additional planets in the system, as well as the composition, tidal decay, tidal distortion, and potential for future observations of TOI-2431 b. We conclude with a summary of our findings in Section 7.

2. Observations and Data Reduction

2.1. TESS Photometry

TOI-2431 was observed by TESS in Sectors 31, 42, 43, 70, and 71 at a cadence of two minutes between 2020 and 2023. The TESS Science Processing Operations Center (SPOC, Jenkins et al. 2016) pipeline identified a small transit signal with a periodicity of ~ 5 hours. We downloaded, and combined the available light curves using the *lightcurve* package (Lightcurve Collaboration et al. 2018). We worked with the Presearch Data Conditioning Simple Aperture Photometry (PDCSAP) SPOC light curves, which are corrected for pointing and focus-related instrumental signatures, discontinuities resulting from radiation events in the CCD detectors, outliers, and flux contamination. Figure 1 shows the TESS pixels used for the PDC light curve generated with the *tpfplotter* code². The TESS light curve, along with the best transit model, is shown in Section 4.1.1.

2.2. Radial Velocities with NEID and HPF

To constrain the mass of TOI-2431 b, we obtained high precision RVs using the NEID spectrograph (Schwab et al. 2016) on the WIYN 3.5m Telescope³ at Kitt Peak National Observatory in Arizona. In total, we obtained 12 NEID exposures between December 17, 2024, and February 19, 2025. The exposure time for all observations was 5 minutes. The S/N varied per observation, with the median S/N of 27 at 860 nm.

² <https://github.com/jlillo/tpfplotter>

³ The WIYN Observatory is a joint facility of the NSF National Optical-Infrared Astronomy Research Laboratory, Indiana University, the University of Wisconsin-Madison, Pennsylvania State University, and Princeton University.

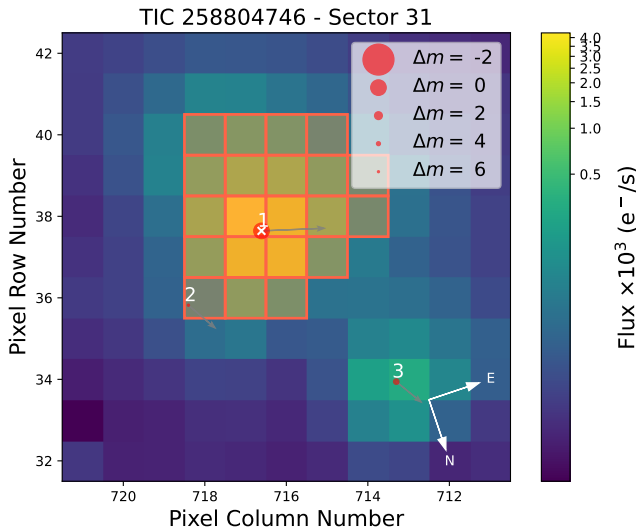


Fig. 1. TESS target pixel file image of TOI-2431 in Sector 31. The electron fluxes are shown with the color bar. The red-bordered pixels highlight the pixels used for the PDCSAP light curve. The TESS pixel scale is approximately $21''$. The size of the red circles indicates the TESS magnitudes of all nearby stars and TOI-2431 (white cross). Gray arrows show the proper motion directions of the stars in the field.

The NEID spectra were first extracted using the NEID Data Reduction Pipeline (DRP⁴; Bender et al. 2022). These spectra were downloaded from the NEID archive⁵. We then extracted radial velocities from NEID using the NEID-SERVAL code, a spectral-matching code that builds on the SpEctrum Radial Velocity AnaLyzer (SERVAL; Zechmeister et al. 2018) code and which has been adapted for NEID data (Stefansson et al. 2022). From this, we obtain a median RV precision of 2.9 m s^{-1} .

In addition to the NEID data, to constrain the stellar parameters of the host star, we also obtained spectra of TOI-2431 with the Habitable-zone Planet Finder (HPF) Spectrograph (Mahadevan et al. 2012) on the 10m Hobby-Eberly Telescope (HET, Ramsey et al. 1988; Hill et al. 2021) at McDonald Observatory in Texas. We obtained three observations between December 29, 2024, and February 9, 2025, using ~ 15 minute exposures. For these observations, the median S/N is 205 at $1 \mu\text{m}$ with the median RV precision of 7.3 m s^{-1} .

The HPF 1D spectra were first reduced and extracted using the HPF pipeline, following the procedures outlined in Ninan et al. (2018), Kaplan et al. (2019), and Metcalf et al. (2019). We extracted the radial velocities using HPF-SERVAL following Stefansson et al. (2020) and Stefansson et al. (2023). The RVs of TOI-2431 are listed in Table A.1.

2.3. Speckle Imaging

To rule out the presence of nearby stars to TOI-2431, we observed TOI-2431 using the NESSI speckle imager (Scott et al. 2018) on the WIYN 3.5m Telescope at Kitt Peak in Arizona in two bands: the 562 nm band (width of 44 nm), and the 832 nm band (width of 40 nm; Scott et al. 2018) available on NESSI. Figure 2 shows the reconstructed images in both bands along with the corresponding 5σ contrast curve. The figure shows that no

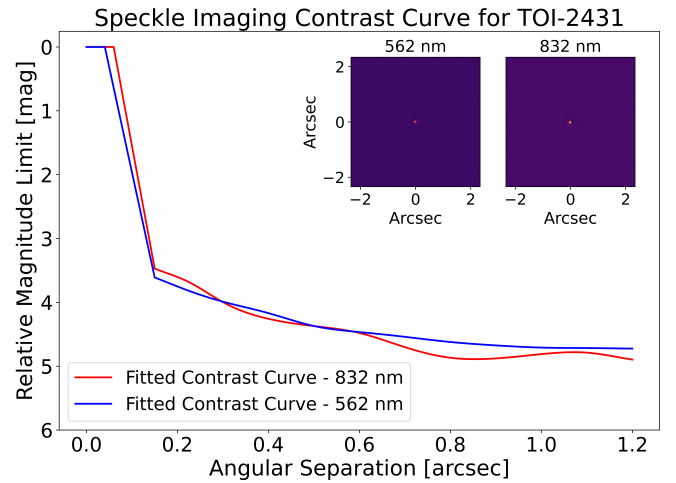


Fig. 2. Results from NESSI speckle imaging of TOI-2431. The plot shows the contrast curve as observed in the NESSI 562nm filter (blue curve), and the 832nm filter (red). The inset images highlight 256×256 insets of the reconstructed images. No secondary companions are seen. Note that in this figure, $1''$ corresponds to 36 AU at the distance of TOI-2431 b.

secondary sources were detected near (between $0.2''$ and $1.2''$) the host star.

TOI-2431 is a high proper motion star, with a total proper motion of $384.5 \text{ mas yr}^{-1}$ ($\mu_\alpha = 374.9 \text{ mas yr}^{-1}$, $\mu_\delta = -85.7 \text{ mas yr}^{-1}$; Gaia Collaboration et al. 2023). Thus, to rule out any background star contamination as TOI-2431 moves across the sky, we also inspected the movement of TOI-2431 as a function of time, as seen in Fig. 3. For this, we have used the First Palomar Sky Survey (POSS-I; Deacon et al. 2009) image taken in 1954 and an image taken by the Zwicky Transient Facility (ZTF; Masci et al. 2019) in 2018. To compare the images, we have also highlighted the position of TOI-2431 as measured by Gaia (Gaia Collaboration et al. 2023) at the Gaia J2016 epoch. The comparison showed that TOI-2431 has moved substantially from 1954 to 2018, and there are no background stars around it that could affect our interpretation.

3. Stellar Parameters

3.1. Spectroscopic and Model Dependent Stellar Parameters

We used the HPF-SpecMatch code (Stefansson et al. 2020) to constrain the stellar effective temperature (T_{eff}), surface gravity ($\log g$), and metallicity ($[\text{Fe}/\text{H}]$) of TOI-2431. HPF-SpecMatch compares an observed spectrum of a target star with a library of high S/N HPF spectra of well-characterized stars. For the analysis, we follow Stefansson et al. (2020), and use the 5th HPF spectral order, which spans $8534\text{--}8645 \text{ \AA}$, as this order is the HPF order that is minimally impacted by telluric and sky-emission line contamination. Using HPF-SpecMatch, we obtain $T_{\text{eff}} = 4080 \pm 77 \text{ K}$, $\log g = 4.68 \pm 0.05$, and $[\text{Fe}/\text{H}] = -0.02 \pm 0.13 \text{ dex}$, where the uncertainties are obtained with the cross-validation approach outlined in Stefansson et al. (2020) and Jones et al. (2024).

To obtain model-dependent estimates of the other stellar parameters of interest—including the mass, radius, and age of the host star—we made use of the ARIADNE code (Vines & Jenkins 2022) to fit the Spectral Energy Distribution (SED) of the host star. To fit the SED, ARIADNE uses the Bayesian Model Averag-

⁴ <https://neid.ipac.caltech.edu/docs/NEID-DRP/>

⁵ <https://neid.ipac.caltech.edu/search.php>

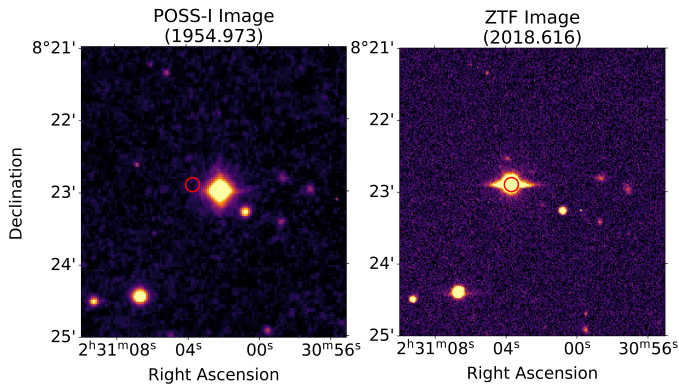


Fig. 3. Movement of TOI-2431 as a function of time. The left image shows a POSS-I image of TOI-2431 (middle star) taken in 1954, and the right image shows a ZTF image of TOI-2431 taken in 2018. The red circle highlights the position of TOI-2431 as measured by Gaia at the Gaia J2016 epoch. Due to its high proper motion, TOI-2431 has moved substantially between the two images, highlighting that there is no background star seen in the vicinity of TOI-2431 that could confound the planet interpretation of TOI-2431 b.

ing technique on a suite of different possible stellar models. For the fit, we used the *Phoenix* v2 (Husser et al. 2013), *BT-Settl* (Allard et al. 2012), Kurucz (1993), and Castelli & Kurucz (2003) stellar atmospheric models. We have also placed informative priors on T_{eff} , $[\text{Fe}/\text{H}]$, and $\log g$, from the HPF-SpecMatch analysis above. Given the close proximity of the star, we assumed that the optical interstellar extinction was negligible and set the corresponding extinction parameter A_v to zero. Within ARIADNE we adopted the default ARIADNE priors on the stellar radius (broad uniform prior ranging from $0.05 R_{\odot}$ to $100 R_{\odot}$), and the distance to the system (informative gaussian derived by Bailer-Jones et al. 2021). We list the best-fit parameters obtained from the fit in Table 1. The stellar age and isochrone mass are calculated by ARIADNE using the best-fit parameters and the photometric data as input for a MIST isochrone interpolation (Dotter 2016). Lastly, ARIADNE cross-matches the best fit effective temperature to the spectral type table described by Pecaut & Mamajek (2013) to find the spectral type of the star.

3.2. Stellar activity

The S/N of the NEID spectra are not sufficient to recover the Ca II H & K S-value and $\log R'_{HK}$ activity indicators, so we can not use these to estimate expected RV jitter due to magnetic activity (Wright 2005; Isaacson & Fischer 2010; Luhn et al. 2020). However, we note that none of H α or the three Ca II NIR triplet lines is seen to be in emission, indicating that this star is inactive. Further, the TESS photometry does not show evidence of rotational modulation, which is broad agreement with the lack of detection of a clear rotational broadening in the HPF and NEID spectra ($v \sin i_{\star} < 2 \text{ km s}^{-1}$). Together, these support that TOI-2431 is a slowly rotating star for which we do not expect strong rotational modulation in RVs, especially not on timescales close to those of the periodicity of the planet (~ 5 hours).

4. Joint Transit and RV Analysis

4.1. Joint Fits of Transit and RV Observations

To confirm the planetary nature of TOI-2431 b and to better constrain its parameters, we performed joint fits of all of the available transit and RV data using the *juliet* code (Espinoza et al. 2019). *juliet* uses the *batman* code (Kreidberg 2015) for the transit model, *radvel* (Fulton et al. 2018) for the RV model, *celerite* (Foreman-Mackey et al. 2017) for the Gaussian Process (GP) modelling, and *dynesty* (Speagle 2020) for the dynamic nested sampling. We assumed that TOI-2431 b has a circular orbit ($e = 0$), as we expect the orbit to circularize on a short timescale due to tidal interactions with its host star. Additionally, as the TESS Contamination Ratio is low at 0.0011 (Jenkins et al. 2016), we assume no additional dilution of the transit due to nearby stars, and fix the dilution factor for all TESS photometry to unity in all of our fits. We have also tried TESS-Gaia Light Curve (TGLC; Han & Brandt 2023) fit, which resulted in transit depths that are consistent within 1σ of the TESS light curve fit. To account for correlated noise in the TESS data, in all of the fits, we used a GP model with a Matern-3/2 kernel as implemented in the *celerite* code (Foreman-Mackey et al. 2017). Additionally, for the joint fits, we placed an informative prior on the stellar density of $\rho_{\star} = 3.230 \pm 0.180 \text{ g/cm}^3$ (see Table 1).

As a separate test, we performed similar fits with two additional codes: with the *ironman* code (Espinoza-Retamal et al. 2023a, 2024), and with the *ExoMUSE*⁶ code, a code that we have developed that uses *radvel* and *batman* but uses Markov-Chain Monte-Carlo sampling using the *emcee* package (Foreman-Mackey et al. 2013) instead of nested sampling. All fits resulted in consistent parameters within $\sim 1\sigma$, and we elected to adopt the parameters we obtained using the *juliet* code.

We tested fitting the available NEID RV data assuming a single Keplerian, using informative priors on the orbital period of the planet and the transit midpoint from the TESS data. However, this resulted in a residual RV RMS scatter of 9.2 m s^{-1} that is substantially higher than that expected from the median NEID RV uncertainty of 2.9 m s^{-1} . Since the star shows no clear signs of activity and USP planets are often found in multi-planet systems (Winn et al. 2018), this may suggest the presence of additional non-transiting planets in the system.

As highlighted in Section 6.1, we looked for evidence of additional planets in both the TESS data using a box-least-squares analysis, and in the RVs using Generalized Lomb-Scargle (GLS) periodograms, but did not find statistically significant periodic signals in the currently available datasets (Section 6.1 for further details). As highlighted in Section 6.1, we attribute the lack of periodic signals detected in the GLS analysis of the RVs due to the low total number of RVs (12 RVs), and urge additional RV observations to characterize any periodicities in the RV data.

To constrain the mass of TOI-2431 b, we used joint transit and RV fits using two different approaches to account for the excess RV scatter: a) a joint transit and RV fit using the Floating Chunk Offset (FCO) method for the RVs, and b) a joint transit and RV fit employing both i) a Keplerian for the innermost planet, and ii) a quasi-periodic *Gaussian Process* (GP) noise model to account for the excess RV scatter at longer periodicities than the USP. We discuss the results from the two fits below.

⁶ <https://github.com/Kaya-Han-Tas/ExoMUSE>

Table 1. Parameters of TOI-2431. The photometric parameters shown were queried by ARIADNE and used for the SED fit.

Parameter	Description	Value	Source
Main Identifiers			
Gaia DR3 Source ID	-	22707874346819712	Gaia
TIC	TESS Input Catalog Identifier	258804746	TIC
TOI	TESS Object of Interest Identifier	2431	
HIP	Hipparchos Identifier	HIP 11707	HIP
2MASS	2MASS ID	J02310327+0822550	2MASS
Equatorial Coordinates and Proper Motion			
α_{J2016} (RA)	Right Ascension (RA), ICRS epoch 2016.0	02:31:03.68	Gaia
δ_{J2016} (Dec)	Declination (Dec), ICRS epoch 2016.0	08:22:53.85	Gaia
μ_α (mas yr ⁻¹)	Proper motion (RA, mas yr ⁻¹)	374.86 ± 0.024	Gaia
μ_δ (mas yr ⁻¹)	Proper motion (Dec, mas yr ⁻¹)	-85.68 ± 0.018	Gaia
Spectral type	-	K7V	This work
Photometric Magnitudes			
U (mag)	APASS Johnson U magnitude	13.5	APASS
B_{TYCHO} (mag)	TYCHO B magnitude	12.14 ± 0.14	TYCHO
B (mag)	APASS Johnson B magnitude	12.23 ± 0.01	APASS
BP (mag)	Gaia DR3 BP magnitude	11.120 ± 0.003	Gaia
V_{TYCHO} (mag)	TYCHO V magnitude	11.03 ± 0.08	TYCHO
V (mag)	APASS Johnson V magnitude	10.89 ± 0.01	APASS
G (mag)	Gaia DR3 G magnitude	10.325 ± 0.003	Gaia
RP (mag)	Gaia DR3 RP magnitude	9.458 ± 0.004	Gaia
T (mag)	TESS magnitude	9.521 ± 0.006	TESS
J (mag)	2MASS J magnitude	8.36 ± 0.02	2MASS
H (mag)	2MASS H magnitude	7.73 ± 0.05	2MASS
K_S (mag)	2MASS K_S magnitude	7.55 ± 0.02	2MASS
WISE1 (mag)	WISE1 magnitude	7.49 ± 0.03	WISE
WISE2 (mag)	WISE2 magnitude	7.55 ± 0.02	WISE
Stellar Parameters directly Derived by SED fitting			
T_{eff} (K)	Effective temperature	4109^{+28}_{-27}	This work
$\log g$ (cgs)	Stellar gravity	4.68 ± 0.05	This work
[Fe/H] (dex)	Stellar metallicity	-0.02 ± 0.13	This work
Derived Stellar Parameters			
$M_{\star, \text{iso}}$ (M_\odot)	Stellar (Isochrone) Mass	$0.661^{+0.021}_{-0.024}$	This work
R_\star (R_\odot)	Stellar radius	0.651 ± 0.012	This work
L_\star (L_\odot)	Luminosity	0.109 ± 0.005	This work
A_v (mag)	Visual extinction	0.0 (Fixed)	This work
d (pc)	Distance	$36.01^{+0.06}_{-0.02}$	This work
ω (mas)	Parallax	$27.76^{+0.02}_{-0.03}$ mas	This work
Age (Gyr)	Stellar age	$2.0^{+9.1}_{-1.7}$	This work
ρ_\star (g cm ⁻³)	Stellar density	$3.23^{+0.18}_{-0.18}$	This work
Other Stellar Parameters			
$v \sin i_\star$ (km s ⁻¹)	Rotational velocity	< 2	This work
RUWE	Gaia Renormalized Unit Weight Error	1.070	Gaia

Notes. References: Gaia (2016; 2018; 2023), TESS (Stassun et al. 2019, 2018), 2MASS (Skrutskie et al. 2006), WISE (Wright et al. 2010), APASS (Munari et al. 2014), TYCHO (Høg et al. 2000), HIP (Perryman et al. 1997)

4.1.1. Joint fit employing the Floating Chunk Offset (FCO) Method

As USP planets tend to be found in multi-planetary systems, which could cause the RV data to be scattered in excess of the USP RV orbit, an often-used technique to account for the additional RV scatter is the *Floating Chunk Offset (FCO)* method. The method was originally used by Hatzes et al. (2010) to measure the mass of CoRoT-7b, an USP planet with a 0.85 day period, and since then, has been used to measure the masses for multiple short-period planets in the presence of other signals (Hatzes 2014; Deeg et al. 2023; Dai et al. 2024).

The FCO method requires multiple observations to be taken over a single night spanning orbital phases that cause measurable velocity differences. It assumes a Keplerian RV orbit for the innermost planet and fits independent RV offsets between successive visits. Therefore, the method assumes that the only RV motion between successive visits (i.e., within a night) is dominated by the Keplerian model, and that the RV impact of other planetary signals are effectively removed by fitting the RV offsets. For TOI-2431 b, since the period is only 5.4 hours, we obtained 8 RV observations in three different visits, which had typical time-baseline of ~1-2 hours within a visit, with a total time-baseline of ~64 days.

We further note that although we do not expect significant RV variability on the rotational time scale for TOI-2431 given that it is an inactive star (Section 3.2), the FCO method will also remove any activity-driven RV signals at the stellar rotation period. Further, as TOI-2431 is an inactive star, we expect any sources of stellar variability within a night (e.g., oscillations, granulation) that would be retained via the FCO method are also expected to be small, and much less than the median RV uncertainty of the NEID data of 2.9 m s^{-1} .

We implemented the FCO method in our joint fits by defining different nights of observations as different "instruments" that had different systematic velocities called NEID1, NEID2, and NEID3. We tried letting the jitter terms float, however, as the RV variation between the different nights is effectively removed by the different RV offsets, the jitter terms had posteriors consistent with zero. As both different runs resulted in the same planet parameter posteriors, we elected to adopt the simpler fit that fixed the jitter terms to zero.

As we only had three NEID visits to include for the FCO fit, we performed systematic injection and recovery tests to test the robustness of our FCO implementation, which we highlight in Appendix B. In short, we took our observed NEID timestamps, and injected 1,500 synthetic RV signals of two planets: of a USP planet with the same ephemerides as TOI-2431 b, and another longer-period planet with a period in excess of one day. As highlighted in Appendix B, the known RV amplitude is recovered at the rate as expected, we conclude that our FCO implementation and our mass constraint of TOI-2431 b is robust.

The final joint fit is shown in Figure 4, and the resulting best-fit parameters and associated priors are shown in Table 2.

4.1.2. Joint fit employing a Quasi-periodic Gaussian Process

In addition to the FCO fit discussed above, we performed a joint transit and RV fit where we used a Gaussian Process (GP) noise model with a quasi-periodic kernel to account for the excess RV scatter and the possible longer-term RV signals. To do so, we placed a uniform prior on the periodicity of the quasi-periodic GP from 1 to 100 days, to ensure it was substantially longer than the $\sim 5\text{h}$ period of the Keplerian USP component of the model. To provide the best constraint on the mass, for this fit, we used all of the available NEID RVs along with the HPF RVs. Here we note that NEID RVs are more precise than HPF since NEID has higher RV information content on bright K dwarfs than HPF. We let the instrument RV jitters for both instruments float. For consistency, the rest of the priors were kept the same as for the FCO joint fit priors. Table 2 lists the priors and the resulting posterior parameters from the fit, and the resulting GP fit is shown in Figure 5.

5. Results

The results from the FCO joint fit, and the GP joint fits are shown in Figures 4, and 5, respectively, and Table 2 lists the resulting posteriors from both fits.

The FCO joint fit yields a RV semi-amplitude of $8.3_{-1.6}^{+1.5} \text{ m s}^{-1}$, and a mass of $6.2_{-1.2}^{+1.2} M_{\oplus}$. In comparison, the GP joint fit yields an RV semi-amplitude of $6.8_{-2.0}^{+2.1} \text{ m s}^{-1}$, and a mass of $5.1_{-1.5}^{+1.6} M_{\oplus}$. Both the RV semi-amplitude and mass values are consistent within their 1σ uncertainties, as are the other posterior values, as shown in Table 2. As the FCO fit is a simpler fit, with fewer free parameters (one parameter for the Keplerian and three RV offsets, compared to one Keplerian parameter, two RV

offsets, two RV jitter terms, and four parameters for the GP), we elect to adopt the values for the FCO fit. This constrains the mass of the planet at $\sim 5.2\sigma$ confirming TOI-2431 b as a USP planet.

From Table 2, we see that the FCO joint fit results in a planet radius of $1.536_{-0.033}^{+0.033} R_{\oplus}$. This suggests a density of $9.4_{-1.8}^{+1.9} \text{ g cm}^{-3}$, which is slightly denser, but consistent with an Earth-like composition.

6. Discussion

6.1. Search for Additional Planets

To search for evidence of additional transiting planets in the TOI-2431 system, we used the Box-Least Square (BLS) algorithm as implemented in the *lightcurve* package (Lightcurve Collaboration et al. 2018). The resulting BLS periodogram is shown in Figure 6. We do not observe any clear signal in the BLS other than the signals corresponding to TOI-2431 b and its aliases. Further, when removing that signal, no additional signals with a Signal Detection Efficiency (SDE) larger than 10 are detected. We see a potential signal with a period of ~ 14 days and an SDE of ~ 9 , but we attribute this to the combined effect of the gaps in the TESS data (the signal is close to half of the TESS baseline per sector) and the masking of TOI-2431 b transits, which removed a significant number of data points. Therefore, we conclude there are no clear signs of additional transiting planets in the system. The lack of detection of other transiting planets is not unexpected, as the planets in USP systems tend to have a high mutual inclinations (Dai et al. 2018), which together with the high period ratios between neighboring planets (Dai et al. 2015) can easily explain the non-detection of additional transiting planets in the system.

To look for evidence of non-transiting planets in the RVs, we show a Generalized Lomb-Scargle (GLS) Periodogram of the NEID RVs along with the accompanying window function in Figure 7. We highlight the orbital period of TOI-2431 b's with the red vertical dashed line, and we highlight half of the orbital period with the blue vertical dashed line. The latter has a False Alarm Probability (FAP) $< 1\%$ (grey horizontal line), which we attribute being likely due to TOI-2431 b. The window function shows that these peaks do not originate from an artifact due to sampling. The grey dotted line shows that we do not detect any additional significant periodicities with $\text{FAP} < 1\%$. We attribute this being due to the low number of RVs, as periodogram analyses like these benefit from higher number of datapoints, especially in the absence of extremely clear sinusoidal signals. Given the high RV scatter compared to expectations from a single Keplerian, we urge additional RV observations of the system to look for evidence of significant additional periodicities to reveal additional planets in the TOI-2431 system.

In addition to RVs, massive longer-period exoplanets might be detected using astrometry. The star is included in the Hipparcos-Gaia Catalog of Accelerations (Brandt 2021). However, we do not see any significant proper motion differences, ruling out massive companions at large orbital distances. Nonetheless, future Gaia DR4 astrometry can put more constraints on possible outer companions at intermediate orbital distances of $\sim 3\text{--}5 \text{ AU}$ (Perryman et al. 2014). The star is relatively nearby ($d \sim 36 \text{ pc}$) and bright ($G \sim 10.3$), which increases the likelihood of detecting massive outer companions to TOI-2431 b with Gaia (and possibly measuring the mutual inclination between the planetary orbits; Espinoza-Retamal et al. 2023b).

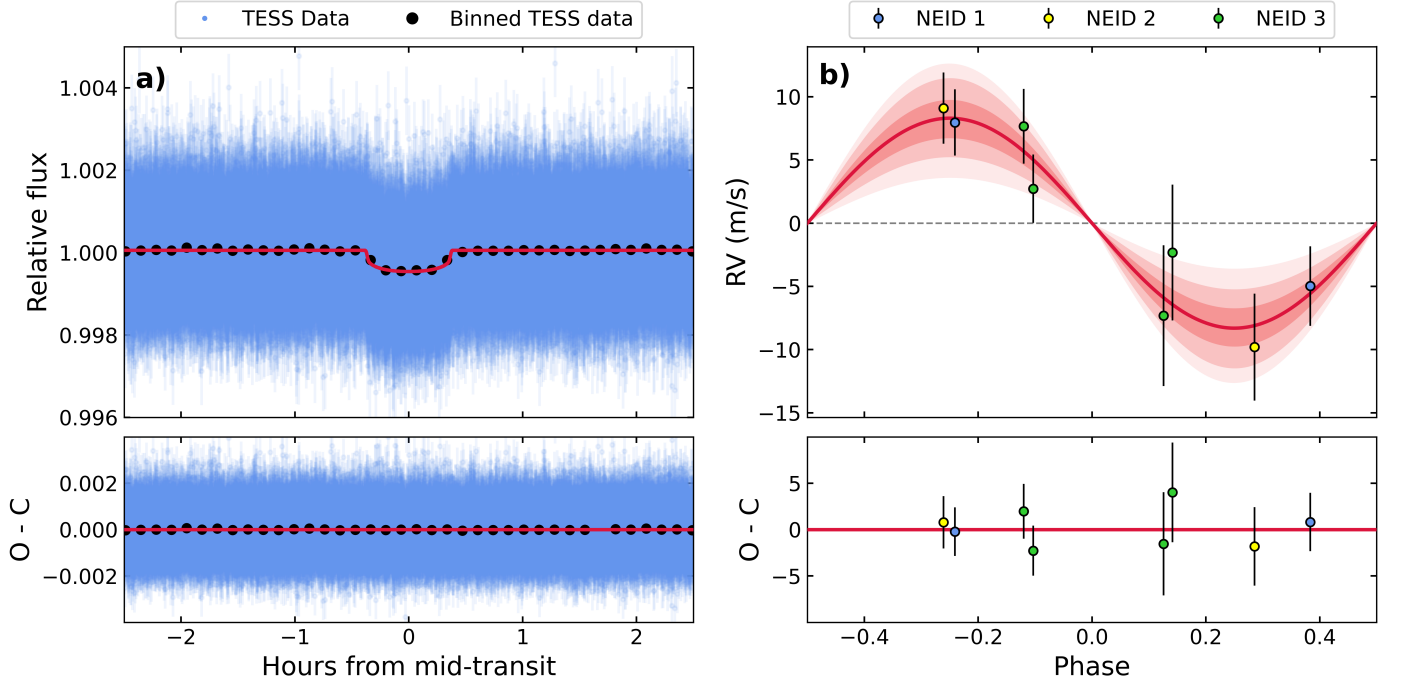


Fig. 4. Best fit results from a joint transit and RV fit using the Floating Chunk Offset (FCO) method for the RV data. **a)** *Top*: Detrended TESS photometric observations (2 min exposures) are shown in blue folded on the time of transit. Best-fit transit model is shown in red. The black points show the TESS data binned to a cadence of 2 min. *Bottom*: Residuals from the best-fit model. **b)** *Top*: Phase-folded RV data and best-fit model (red) of TOI-2431 as observed with NEID in three separate visits listed as NEID1 (blue), NEID2 (yellow), and NEID3 (green). The red shaded regions show the 1, 2, and 3σ credible intervals of the best-fitting model. *Bottom*: Residuals from the best-fit model. We adopt the values from this fit as the values for TOI-2431 b.

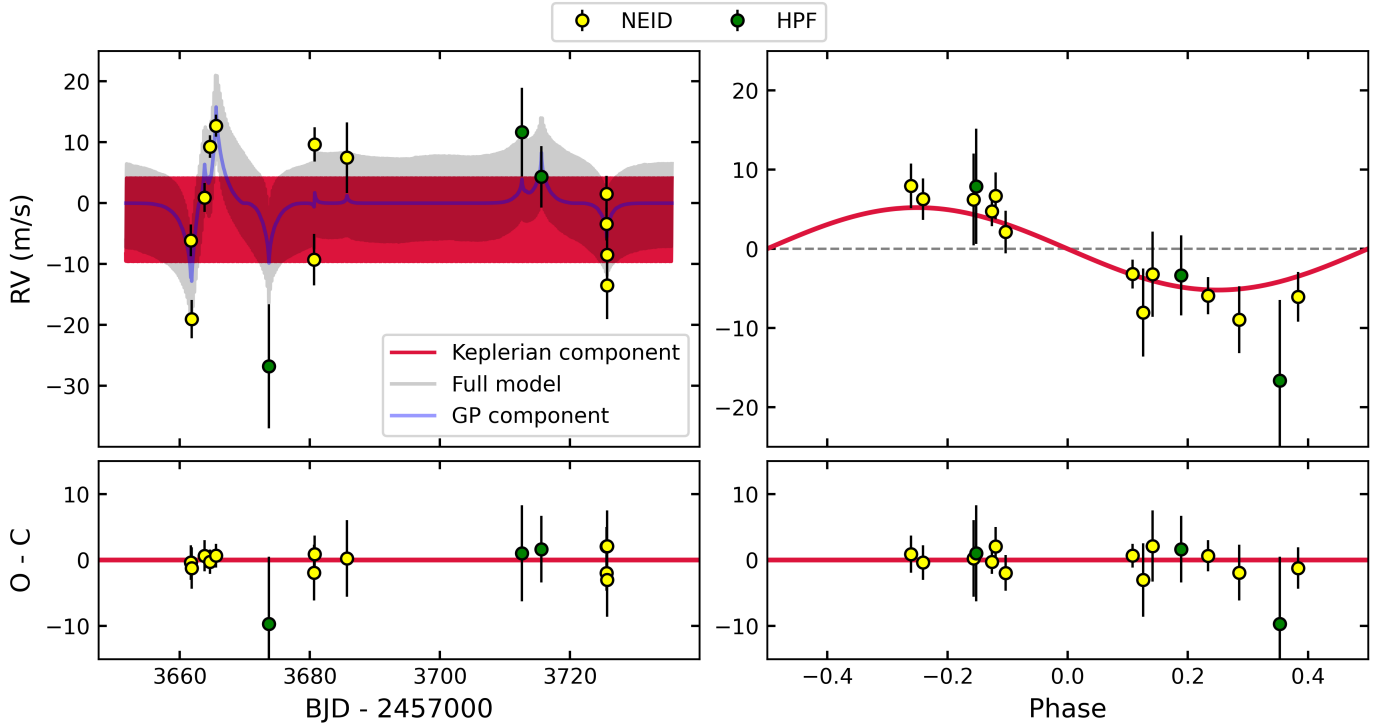


Fig. 5. Best fit results from a joint transit and RV fit using a quasi-periodic GP model to account for the excess RV scatter in the RVs. **a)** *Top*: NEID (yellow) and HPF (green) RVs as a function of time. The best-fit Keplerian model is shown in red (appears as a solid band due to the short period orbit). The median of the GP component is shown in blue. The joint best-fit model is shown in grey. *Bottom*: Residuals from the best fit model. **b)** *Top*: Phase-folded RVs on the period of TOI-2431 b. Best fit Keplerian model after subtracting the GP model is shown in red. *Bottom*: RV residuals as a function of phase.

Table 2. Derived Parameters of TOI-2431 b from a joint analysis of the available transit and radial velocity data. $\mathcal{N}(\mu, \sigma)$ denotes a normal prior with mean (μ) and standard deviation (σ), $\mathcal{U}(a, b)$ denotes a uniform prior with a start value (a) and an end value (b), and $\mathcal{L}(\mu, \sigma)$ denotes a log-normal prior with mean (μ) and standard deviation (σ). The posteriors from the Floating Chunk Offset (FCO) fit and the Gaussian Process (GP) fit are consistent.

Parameter	Description	Prior Distribution	Posterior Distribution (FCO Fit, adopted)	Posterior Distribution (GP Fit)
MCMC Input Parameters:				
P (days)	Orbital Period	$\mathcal{N}(0.224195, 4 \times 10^{-7})$	$0.22419577^{+5 \times 10^{-8}}_{-5 \times 10^{-8}}$	$0.22419578^{+5 \times 10^{-8}}_{-5 \times 10^{-8}}$
T_0 (BJD)	Time of Transit (BJD - 2460000)	$\mathcal{N}(258.8689, 4.6 \times 10^{-4})$	$258.8685^{+0.00015}_{-0.00015}$	$258.8685^{+0.00016}_{-0.00015}$
e	Eccentricity	0 (Adopted)	0 (Adopted)	0 (Adopted)
ω (deg)	Argument of Periapsis	90 (Adopted)	90 (Adopted)	90 (Adopted)
b	Impact Parameter	$\mathcal{U}(0, 1)$	$0.574^{+0.033}_{-0.031}$	$0.572^{+0.033}_{-0.035}$
K (m s $^{-1}$)	RV Semi-Amplitude	$\mathcal{U}(0, 1000)$	$8.3^{+1.5}_{-1.6}$	$6.8^{+2.1}_{-2.0}$
q_1	TESS Limb Darkening Coefficient	$\mathcal{U}(0, 1)$	$0.55^{+0.22}_{-0.18}$	$0.59^{+0.23}_{-0.19}$
q_2	TESS Limb Darkening Coefficient	$\mathcal{U}(0, 1)$	$0.24^{+0.28}_{-0.16}$	$0.23^{+0.26}_{-0.16}$
$m_{\text{dilution, TESS}}$	Dilution Factor of TESS	1 (Adopted)	1 (Adopted)	1 (Adopted)
$m_{\text{flux, TESS}}$	Offset Relative Flux	$\mathcal{N}(0.0, 0.1)$	$-0.000057^{+0.000031}_{-0.000032}$	$-0.00006^{+0.00003}_{-0.00003}$
$\text{GP}_{\sigma, \text{TESS}}$ (ppm)	Amplitude of the GP	$\mathcal{L}(10^{-6}, 10^6)$	$0.00027^{+0.000020}_{-0.000017}$	$0.00027^{+0.000019}_{-0.000017}$
$\text{GP}_{\rho, \text{TESS}}$ (ppm)	Length-Scale of the Matern Kernel	$\mathcal{L}(10^{-6}, 10^6)$	$0.68^{+0.087}_{-0.078}$	$0.68^{+0.084}_{-0.078}$
σ_{TESS} (ppm)	Light Curve Jitter	$\mathcal{L}(10^{-6}, 10^6)$	$177^{+9.8}_{-10}$	$176^{+9.8}_{-10}$
$\text{GP}_{B, \text{RV}}$ (m s $^{-1}$)	Amplitude of the GP (RV)	$\mathcal{L}(10^{-6}, 10^6)$	—	137^{+179}_{-65}
$\text{GP}_{C, \text{RV}}$	Constant Scaling Term of the GP	$\mathcal{L}(10^{-6}, 10^6)$	—	0.40^{+7620}_{-40}
$\text{GP}_{L, \text{RV}}$	Char. Time-Scale of the GP	$\mathcal{L}(10^{-3}, 10^3)$	—	$1.6^{+6.8}_{-1.3}$
$\text{GP}_{P_{\text{rot}}, \text{RV}}$ (days)	Period of the Quasi-Periodic GP	$\mathcal{U}(1, 100)$	—	47^{+35}_{-31}
R_p/R_*	Radius Ratio	$\mathcal{U}(0, 1)$	$0.02133^{+0.00033}_{-0.00031}$	$0.02128^{+0.00036}_{-0.00032}$
ρ_* (g cm $^{-3}$)	Density of Star	$\mathcal{N}(3.23, 0.18)$	$3.24^{+0.18}_{-0.18}$	$3.24^{+0.18}_{-0.18}$
$v_{\gamma, \text{obs, log}}$ (m s $^{-1}$)	Systematic Velocity (NEID, GP)	$\mathcal{U}(-50, 50)$	—	$-2.7^{+5.4}_{-5.5}$
$v_{\gamma, \text{HPF}}$ (m s $^{-1}$)	Systematic Velocity (HPF, GP)	$\mathcal{U}(-50, 50)$	—	$1.3^{+8.9}_{-9.5}$
$v_{\gamma, 1}$ (m s $^{-1}$)	Systematic Velocity (NEID 1)	$\mathcal{U}(-50, 50)$	$-17^{+2.0}_{-2.1}$	—
$v_{\gamma, 2}$ (m s $^{-1}$)	Systematic Velocity (NEID 2)	$\mathcal{U}(-50, 50)$	$-2.3^{+2.4}_{-2.4}$	—
$v_{\gamma, 3}$ (m s $^{-1}$)	Systematic Velocity (NEID 3)	$\mathcal{U}(-50, 50)$	$-9.0^{+1.9}_{-1.8}$	—
$\sigma_{\text{RV, NEID}}$ (m s $^{-1}$)	RV Jitter (NEID, GP)	$\mathcal{L}(10^{-6}, 10^6)$	—	$0.0047^{+0.63}_{-0.0046}$
$\sigma_{\text{RV, HPF}}$ (m s $^{-1}$)	RV Jitter (HPF, GP)	$\mathcal{L}(10^{-6}, 10^6)$	—	$0.0069^{+2.2}_{-0.0069}$
$\sigma_{\text{RV, 1}}$ (m s $^{-1}$)	RV Jitter (NEID 1)	0 (Adopted)	0 (Adopted)	0 (Adopted)
$\sigma_{\text{RV, 2}}$ (m s $^{-1}$)	RV Jitter (NEID 2)	0 (Adopted)	0 (Adopted)	0 (Adopted)
$\sigma_{\text{RV, 3}}$ (m s $^{-1}$)	RV Jitter (NEID 3)	0 (Adopted)	0 (Adopted)	0 (Adopted)
Derived Parameters:				
M_p (M $_{\oplus}$)	Planet Mass	—	$6.2^{+1.2}_{-1.2}$	$5.1^{+1.6}_{-1.5}$
R_p (R $_{\oplus}$)	Planet Radius	—	$1.536^{+0.033}_{-0.033}$	$1.533^{+0.034}_{-0.033}$
ρ_p (g cm $^{-3}$)	Planet Density	—	$9.4^{+1.9}_{-1.8}$	$7.8^{+2.5}_{-2.4}$
i (deg)	Inclination	—	$74^{+0.99}_{-0.96}$	$74^{+1.1}_{-1.0}$
a (AU)	Semi-Major Axis	—	$0.0063^{+0.0001}_{-0.0001}$	$0.0063^{+0.0001}_{-0.0001}$
ESM	Emission Spectroscopy Metric	—	27	27
$T_{\text{eq, } a=0}$ (K)	Equilibrium Temp. ($A_B = 0$)	—	2063^{+30}_{-30}	2063^{+30}_{-30}
$T_{\text{eq, } a=0.3}$ (K)	Equilibrium Temp. ($A_B = 0.3$)	—	1887^{+28}_{-28}	1887^{+28}_{-28}

6.2. Planet Composition

Figure 8 compares the mass and radius of TOI-2431 b compared to other USP planets (bold points) and other exoplanets (faint points) with well-characterized masses and radii. To examine possible compositions that TOI-2431 b is compatible with, we additionally plot planet composition models from Zeng et al. (2019) as lines of constant density. We see that TOI-2431 b is slightly denser, but compatible with an Earth-like planet composition, similar to other well-characterized USP planets. Due to its close distance to the host star and the high incident irradiation, this results in an equilibrium temperature of 2063 ± 30 K (assuming Bond Albedo as $A_B = 0$). This temperature exceeds the melting points of many common silicate minerals found in plan-

ets, suggesting that the planet’s surface is likely to be partially or fully molten.

6.3. Star-Planet Tidal Interactions

The short orbital period of TOI-2431 b suggests that it is subject to strong tidal interactions with its host star, potentially leading to tidal deformation and orbital decay. We discuss these tidal effects further below, broadly following similar discussions of the USP planets TOI-6255 b (Dai et al. 2024), and TOI-6324 b (Lee et al. 2025).

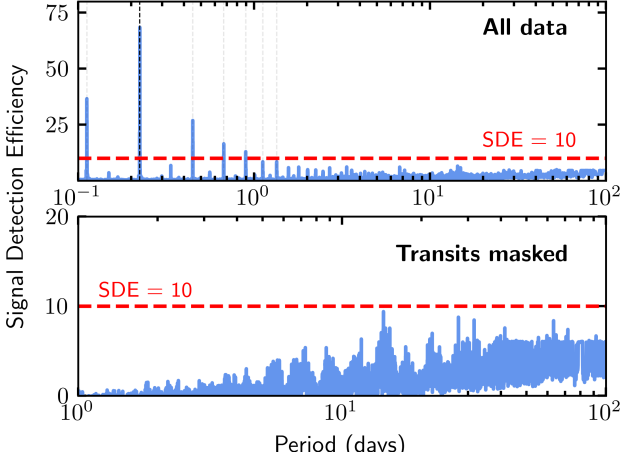


Fig. 6. Box-least square (BLS) periodogram of the TESS data. *Top:* BLS periodogram of all of the TESS sectors. The highest peak reveals the period of TOI-2431 b of 0.22 days, which is highlighted with the black dashed vertical line. Aliases of this period are also shown as faint dashed lines. The horizontal red dashed line shows a Signal Detection Efficiency of 10, the threshold we adopt for a significant signal. *Bottom:* BLS periodogram of the TESS data after masking out the transits of TOI-2431 b. No significant peaks are detected.

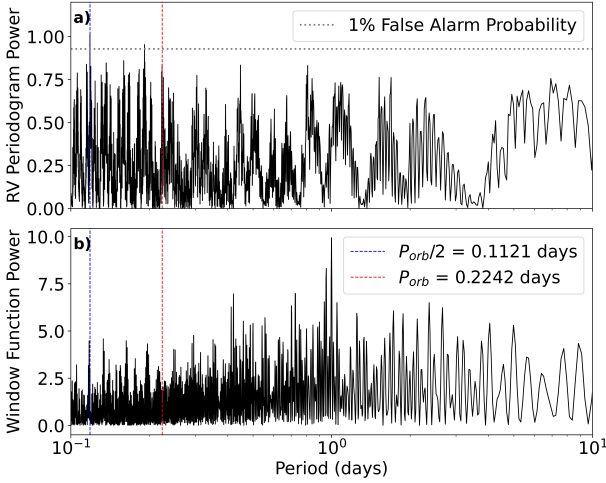


Fig. 7. Generalized Lomb-Scargle (GLS) Periodogram and Window Function of the NEID RVs of TOI-2431 **a)** GLS Periodogram. The grey dotted line represents the False Alarm Probability (FAP) of 1%. The period of TOI-2431 b is highlighted with red vertical dashed line and the half-period is highlighted with blue vertical dashed line. Beyond the peak seen at $P_{\text{orb}}/2$, we see no additional signals with $\text{FAP} < 1\%$. **b)** Window function of the RVs in a).

6.3.1. Proximity to the Roche Limit and Tidal Deformation

The minimum period at which a planet of mean density ρ_p can orbit before being disintegrated by tidal forces is set by the Roche limit. Approximating a planet as an incompressible fluid, this Roche period is given by (Rappaport et al. 2013):

$$P_{\text{Roche}} \approx 12.6 \text{ h} \left(\frac{\rho_p}{1 \text{ g cm}^{-3}} \right)^{-1/2}. \quad (1)$$

Using TOI-2431 b's bulk density of $\rho_p = 9.4^{+1.9}_{-1.8} \text{ g cm}^{-3}$, we estimate $P_{\text{Roche}} = 4.11^{+0.48}_{-0.36} \text{ h}$. Therefore, $P_{\text{orb}}/P_{\text{Roche}} = 1.31^{+0.12}_{-0.14}$,

suggesting that TOI-2431 b has an orbital period only $\sim 30\%$ larger than the Roche limit and that tidal forces are likely to produce measurable effects on the planet.

One possible effect of the proximity of TOI-2431 b to its host star is to tidal deformation, where the shape of the planet is elongated towards the host star. To quantify this effect, we can describe the planet as an elongated ellipsoid parametrized as having three different radii, R_1 , R_2 , R_3 , where R_1 is the radius of the planet along the axis that points towards the host star, R_2 is along the direction of orbit, and R_3 is along the orbit normal. Following Dai et al. (2024), the radii are given by:

$$R_1 = R_{\text{vol}} \left(1 + \frac{7}{6} \delta R_p \right), \quad (2)$$

$$R_2 = R_{\text{vol}} \left(1 - \frac{1}{3} \delta R_p \right), \quad (3)$$

$$R_3 = R_{\text{vol}} \left(1 - \frac{5}{6} \delta R_p \right), \quad (4)$$

where δR_p is the tidal distortion of the planet, and R_{vol} is the volumetric radius of the planet defined as $R_{\text{vol}} \equiv (R_1 R_2 R_3)^{1/3}$. Given its short-period orbit, TOI-2431 b is expected to be tidally locked (Winn et al. 2018), with a rotational period equal to its orbital period, resulting in R_1 being hidden from the observer during transit. The radius that is observed during transit therefore is $R_{\text{tran}} \equiv (R_2 R_3)^{1/2}$, giving rise to the relation,

$$R_{\text{vol}} = R_{\text{tran}} \left(1 + \frac{7}{12} \delta R_p \right). \quad (5)$$

Following Dai et al. (2024), the tidal distortion δR_p can be calculated using

$$\delta R_p = h_2 \zeta, \quad (6)$$

$$\zeta = \frac{M_\star}{M_p} \left(\frac{R_p}{a} \right)^3, \quad (7)$$

where R_p is the planetary radius, h_2 is the Love number, a is the semi-major axis, and M_p and M_\star are the masses of the planet and host star, respectively. Following Dai et al. (2024), we adopt a fiducial $h_2 = 1$, from which we find that TOI-2431 b's volumetric radius is 2.4% larger than the observed transit radius. Further, we find that the difference between the longest axis R_1 and the shortest axis R_3 to be $(R_1 - R_3)/R_1 = 0.087 \pm 0.017$. Putting this value into context with other USPs, Figure 9a shows that, under these assumptions, TOI-2431 b is among the most tidally deformed USP planets, along with TOI-6324 b (Lee et al. 2025), KOI-55 b (Charpinet et al. 2011), and TOI-6255 b (Dai et al. 2024).

6.3.2. Orbital Decay

Tidal interactions also result in energy dissipation, leading to a gradual inward spiral of a planet toward its host star. The tidal decay timescale τ_p , assuming a constant-lag-angle model (Goldreich & Soter 1966; Dai et al. 2024), is given by:

$$\tau_p \equiv \frac{P}{\dot{P}} \approx 30 \text{ Gyr} \left(\frac{Q'_\star}{10^6} \right) \left(\frac{M_\star/M_p}{M_\odot/M_\oplus} \right) \left(\frac{\rho_\star}{\rho_\odot} \right)^{5/3} \left(\frac{P}{1 \text{ day}} \right)^{13/3}, \quad (8)$$

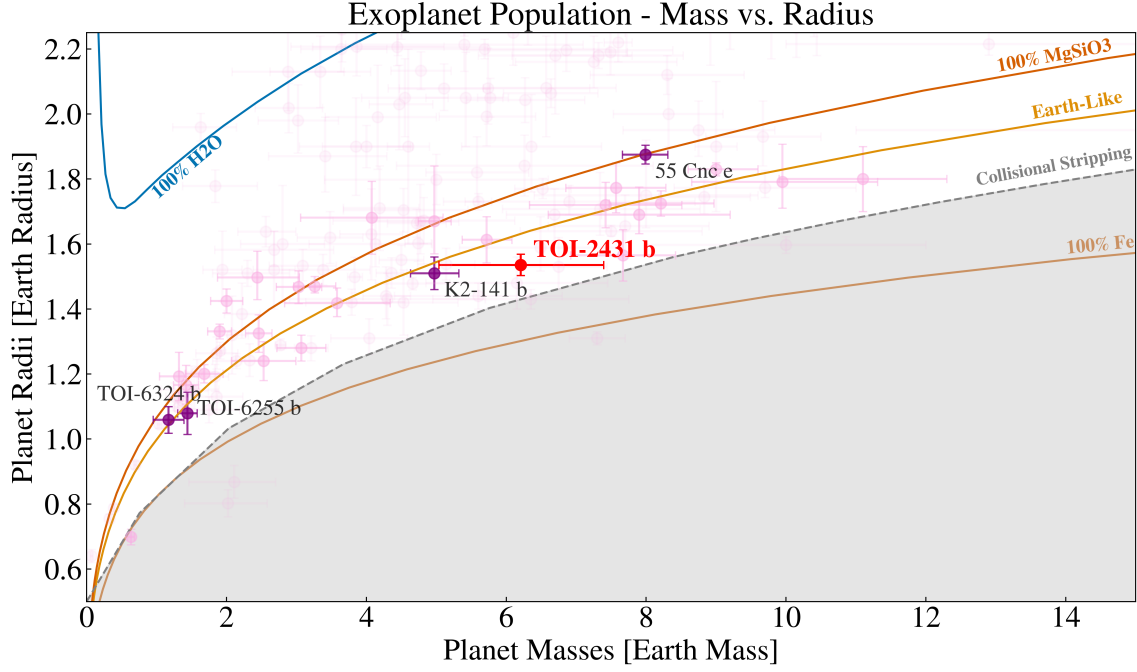


Fig. 8. Planet radius as a function of planet mass along with lines of constant density from (Zeng et al. 2019). The gray shaded region indicates planets with iron content exceeding the maximum value predicted from models of collisional stripping (Marcus et al. 2010). Confirmed USP planets are shown with bold foreground points, and other confirmed exoplanets from the NASA Exoplanet Archive are shown with the faint purple points. TOI-2431 b is shown in red. We only show systems with better than 3σ mass and radius constraints.

where Q'_* is the reduced stellar tidal quality factor and is the main source of uncertainty for this calculation. Following Dai et al. (2024) and Lee et al. (2025), we adopt $Q'_* = 10^7$, representing a relatively slow stellar dissipation rate as empirically found by Penev et al. (2018). From this, we find $\tau_P \approx 200$ Myr for TOI-2431 b, while stressing the underlying uncertainty in the Q'_* value of the star that may differ from the assumed value by more than an order of magnitude and would change the timescale accordingly.

The time it takes to reach the Roche limit can be found by integrating Equation 8, yielding

$$\tau_{Roche} = k \left(\left(\frac{P}{1 \text{ day}} \right)^{13/3} - \left(\frac{P_{Roche}}{1 \text{ day}} \right)^{13/3} \right), \quad (9)$$

where

$$k \approx 7 \text{ Gyr} \left(\frac{Q'_*}{10^6} \right) \left(\frac{M_*/M_p}{M_\odot/M_\oplus} \right) \left(\frac{\rho_*}{\rho_\oplus} \right)^{5/3}, \quad (10)$$

resulting in $\tau_{Roche} \approx 31$ Myr. We compare τ_{Roche} of TOI-2431 b to other well-characterized USPs in Figure 9b—where we assumed a fixed $Q'_* = 10^7$ for all of the systems—from which we see that TOI-2431 b has the shortest τ_{Roche} timescale. This puts TOI-2431 b in a regime where orbital decay could potentially be detectable with long-term observations (see e.g., Wilkins et al. 2017). Such observations will constrain Q'_* and may lead to further insights into the tidal interactions and future evolution of the system.

6.4. Comparison with other USPs and future observations

With a period of only 5.4 hours, TOI-2431 b is among the shortest-period exoplanets discovered to date, but is the shortest period planet with both a well-characterized mass and ra-

dius. The first and second shortest-period planets, PSR J1719-1438 b ($P = 2.2$ h; Bailes et al. 2011) and M62H b ($P = 3.2$ h; Vleeschower et al. 2024), were discovered with the pulsar timing method, which lacks planetary radius measurements. As for the third and fourth shortest-period planets, KOI-1843.03 ($P = 4.2$ h; Rappaport et al. 2013) and K2-137 b ($P = 4.3$ h; Smith et al. 2018), both were discovered by the transit technique, but currently lack robust planet mass measurements. The fifth shortest-period planet, KIC 10001893 b ($P = 5.3$ h; Silvotti et al. 2014), has been discovered with the orbital brightness modulation technique and lacks planetary mass and radius measurements.

The closest exoplanets to TOI-2431 b in terms of period and orbital parameters are TOI-6255 b ($P = 5.7$ h; Dai et al. 2024), and TOI-6324 b ($P = 6.7$ h; Lee et al. 2025), and K2-137 b ($P = 4.3$ h; Smith et al. 2018), which were all first detected using the transit technique. As seen in Figure 10, TOI-2431 b is one of the USP planets that form the lower boundary of the Hot Neptune Desert, which is a sparsely populated region in the exoplanet population (Mazeh et al. 2016).

With its ultra-short period and the brightness of its host star, TOI-2431 b is a promising candidate for phase-curve observations with JWST. Figure 11 shows the Emission Spectroscopy Metric (ESM; Kempton et al. 2018)—which quantifies the feasibility of phase-curve and emission spectroscopic observations with JWST—as a function of orbital period for TOI-2431 b compared to other well-characterized USP planets. TOI-2431 b has an ESM ~ 27 (Table 2), which makes it one of the best rocky planets for phase-curve observations. Such JWST phase curve observations, could shed light onto the presence or absence of a heavy-mean-molecular-weight atmosphere on TOI-2431 b (Dai et al. 2024). In the presence of an atmosphere, JWST's ability to detect thermal emission across a broad wavelength range would allow a probe of the temperature distribution difference between the dayside and nightside of the planet, yielding insight into the

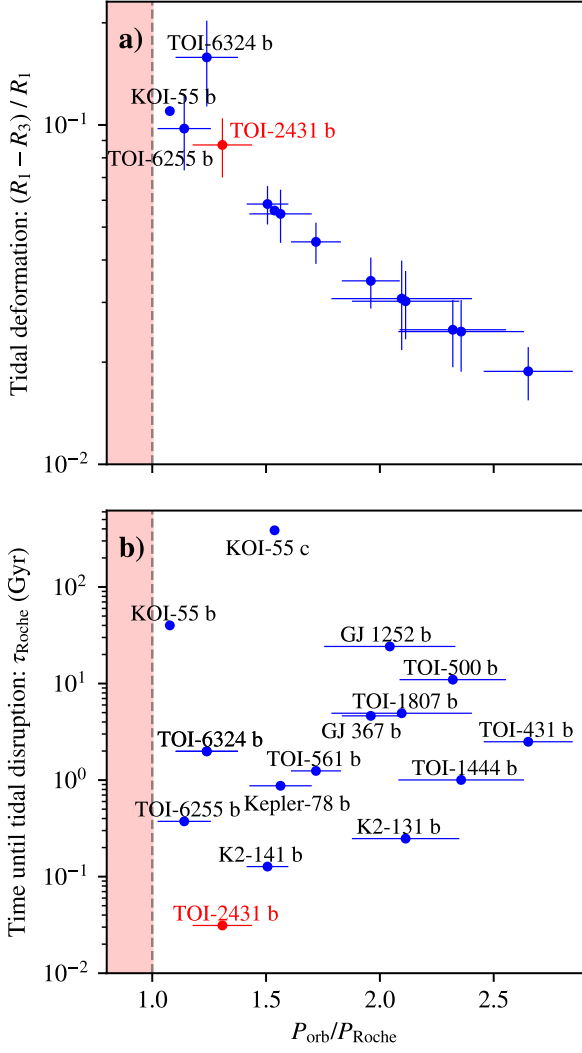


Fig. 9. **a)** Expected tidal deformation of USPs parametrized as $(R_1 - R_3)/R_1$ as a function of $P_{\text{orb}}/P_{\text{Roche}}$. Here the planets are approximated as compressed ellipsoids with primary axes radii of R_1 , R_2 , and R_3 , where R_1 is the radius of the planet pointing towards the star, and R_3 is the radius along the orbit normal. We see that TOI-2431 b is among some of the most tidally distorted USP planets. **b)** Roche limit timescales of USPs as a function of $P_{\text{orb}}/P_{\text{Roche}}$. The latter indicates the proximity to the Roche limit, and the former indicates the timescale to reaching the Roche limit. We see that TOI-2431 b has the shortest timescale until tidal disruption of ~ 31 Myr.

atmospheric circulation of the planet. In the case of no atmosphere, phase curve observations could inform about the planet's surface mineralogy, yielding valuable insights into its composition and evolutionary history (Zilinskas, M. et al. 2022; Zhang et al. 2024; Whittaker et al. 2022).

7. Conclusions

We have confirmed the ultra-short period planet TOI-2431 b using a combination of photometric transit data from TESS, precise RV observations with the NEID and HPF spectrographs, and ground-based speckle imaging with the NESSI instrument. With a period of $P = 0.224$ days, TOI-2431 b is among the shortest period exoplanets detected to date. From a joint analysis the available transit data and RVs, we measure a radius of

$R_p = 1.536 \pm 0.033 R_{\oplus}$, and a mass of $M_p = 6.2 \pm 1.2 M_{\oplus}$, suggesting a bulk density of $9.4^{+1.9}_{-1.8} \text{ g/cm}^3$ which is slightly denser, but consistent with an Earth-like composition. The planet has an equilibrium temperature of $2063 \pm 30 \text{ K}$ (assuming Bond Albedo as $A_B = 0$), suggesting the surface is likely molten. We note that we see evidence of excess scatter in our RV data compared to a single Keplerian planet model, which we interpret as suggestive evidence that there are probably other non-transiting planets in the system. We urge additional RV follow-up observations to gain further insights into other planets in the system.

Additionally, we show that TOI-2431 b is close to its Roche limit with $P_{\text{orb}} \approx 1.31 P_{\text{Roche}}$. Due to its close-in orbit, we show that TOI-2431 b is likely tidally deformed, with its shortest axis being $\sim 9\%$ shorter than its longest axis. Furthermore, assuming a nominal tidal quality factor of $Q'_* = 10^7$, we estimate a tidal decay timescale of only $\tau_{\text{Roche}} \approx 31 \text{ Myr}$, which is the shortest tidal decay timescale compared to other known USPs.

Finally, we show that TOI-2431 b has an ESM of 27, making it one of the best USP planets for phase curve observations with JWST, which could shed light into the surface composition, and if the planet has an atmosphere.

Acknowledgements

This effort started as an observation proposal for granted observation time at the 1.2m Mercator Telescope as part of the La Palma Observing Class at the University of Amsterdam as a group project led by Master's students Kaya Han Taş, Esha Garg, and Syarief N.M. Fariz. The project grew into the current manuscript under the supervision of Gudmundur Stefansson. Esha and Syarief contributed equally to the manuscript. Kaya, Esha, and Syarief thank Antonija Oklopčić, Rudy Wijbrands, Stefanie Fijma, and Nathalie Degenaar for helpful discussions during the observing project.

We acknowledge support from NSF grants AST 1006676, AST 1126413, AST 1310875, AST 1310885, and the NASA Astrobiology Institute (NNA09DA76A) in our pursuit of precision radial velocities in the NIR. We acknowledge support from the Heising-Simons Foundation via grant 2017-0494. This research was conducted in part under NSF grants AST-2108493, AST-2108512, AST-2108569, and AST-2108801 in support of the HPF Guaranteed Time Observations survey. The Hobby-Eberly Telescope is a joint project of the University of Texas at Austin, the Pennsylvania State University, Ludwig-Maximilians-Universität München, and Georg-August Universität Göttingen. The HET is named in honor of its principal benefactors, William P. Hobby and Robert E. Eberly. The HET collaboration acknowledges the support and resources from the Texas Advanced Computing Center. We thank the Resident astronomers and Telescope Operators at the HET for the skillful execution of our observations with HPF.

These results are based on observations obtained with the Habitable-zone Planet Finder (HPF) spectrograph on the HET. The HPF team was supported by grants from the National Science Foundation, the NASA Astrobiology Institute, and the Heising-Simons Foundation.

The Texas Advanced Computing Center (TACC) at the University of Texas at Austin provided high-performance computing, visualization, and storage resources that have contributed to the results reported within this paper.

The Center for Exoplanets and Habitable Worlds and the Penn State Extraterrestrial Intelligence Center are supported by Penn State and its Eberly College of Science.

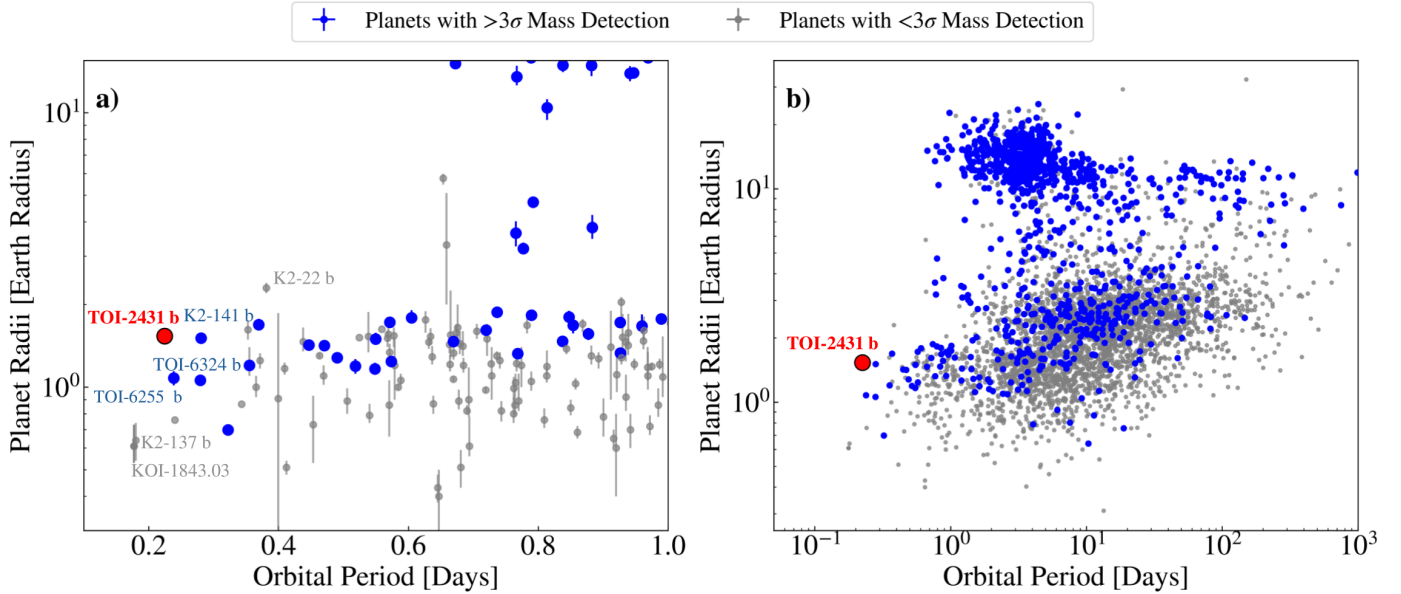


Fig. 10. Planet radius as a function of orbital period for known exoplanets. Confirmed planets with a 3σ or higher precision mass detection are highlighted in blue. The planets that have a mass detection smaller than 3σ precision are shown in gray. TOI-2431 b is shown in red. TOI-2431 b is the shortest period planet with both a characterized mass and radius (better than 3σ). **a)** TOI-2431 b compared to other USPs. **b)** Same as a) but comparing TOI-2431 b to the broader exoplanet population showing that TOI-2431 b is at the lower edge of the Hot Neptune Desert.

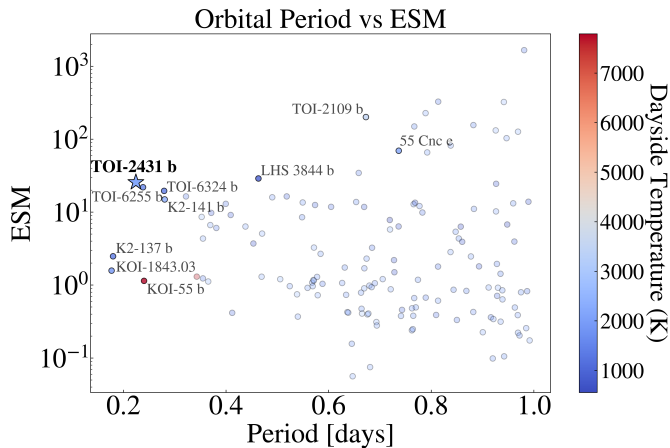


Fig. 11. JWST Emission Spectroscopy Metric (ESM) (Kempton et al. 2018) as a function of planet orbital period for TOI-2431 b and other confirmed USP planets. TOI-2431 b is highlighted with the star, and other well-characterized USPs are shown with the thicker labels. The color bar shows the dayside equilibrium temperature assuming an albedo of $A_B = 0$.

We thank the NEID Queue Observers and WIYN Observing Associates for their skillful execution of our observations. Data presented were obtained by the NEID spectrograph built by Penn State University and operated at the WIYN Observatory by NOIRLab, under the NN-EXPLORE partnership of the National Aeronautics and Space Administration and the National Science Foundation. The NEID archive is operated by the NASA Exoplanet Science Institute at the California Institute of Technology.

Based in part on observations at the Kitt Peak National Observatory (Prop. ID 2025A-546977), managed by the Association of Universities for Research in Astronomy (AURA) un-

der a cooperative agreement with the National Science Foundation. The WIYN Observatory is a joint facility of the NSF's National Optical-Infrared Astronomy Research Laboratory, Indiana University, the University of Wisconsin-Madison, Pennsylvania State University, Purdue University, and Princeton University. The authors are honored to be permitted to conduct astronomical research on Iolkam Du'ag (Kitt Peak), a mountain with particular significance to the Tohono O'odham.

This paper includes data collected by the TESS mission. Funding for the TESS mission is provided by NASA's Science Mission Directorate. This research made use of the NASA Exoplanet Archive and ExoFOP, both of them operated by the California Institute of Technology, under contract with the National Aeronautics and Space Administration under the Exoplanet Exploration Program. This research has made use of the SIMBAD and VIZIER databases at CDS, Strasbourg (France), and of the electronic bibliography maintained by the NASA/ADS system. This work has made use of data from the European Space Agency (ESA) mission Gaia processed by the Gaia Data Processing and Analysis Consortium (DPAC). Funding for the DPAC has been provided by national institutions, in particular the institutions participating in the Gaia Multilateral Agreement.

The research was carried out, in part, at the Jet Propulsion Laboratory, California Institute of Technology, under a contract with the National Aeronautics and Space Administration (80NM0018D0004).

J.I.E.-R. gratefully acknowledges support from the John and A-Lan Reynolds Faculty Research Fund, from ANID BASAL project FB210003, and from ANID Doctorado Nacional grant 2021-21212378. C.I. Cañas acknowledges support by NASA Headquarters through an appointment to the NASA Postdoctoral Program at the Goddard Space Flight Center, administered by ORAU through a contract with NASA.

References

- Adams, E. R., Jackson, B., & Endl, M. 2016, *AJ*, 152, 47
- Akeson, R. L., Chen, X., Ciardi, D., et al. 2013, *PASP*, 125, 989
- Allard, F., Homeier, D., & Freytag, B. 2012, *Philosophical Transactions of the Royal Society A: Mathematical, Physical and Engineering Sciences*, 370, 2765
- Bailer-Jones, C. A. L., Rybizki, J., Fouesneau, M., Demleitner, M., & Andrae, R. 2021, *AJ*, 161, 147
- Bailes, M., Bates, S. D., Bhalerao, V., et al. 2011, *Science*, 333, 1717
- Bender, C., Ninan, J., Terrien, R., et al. 2022, *Bulletin of the AAS*, 54, <https://baas.aas.org/pub/2022n6i401p01>
- Brandt, T. D. 2021, *ApJS*, 254, 42
- Castelli, F. & Kurucz, R. L. 2003, in *Modelling of Stellar Atmospheres*, ed. N. Piskunov, W. W. Weiss, & D. F. Gray, Vol. 210, A20
- Charpinet, S., Fontaine, G., Brassard, P., et al. 2011, *Nature*, 480, 496
- Christiansen, J. L., McElroy, D. L., Harbut, M., et al. 2025, *arXiv e-prints*, arXiv:2506.03299
- Dai, F., Howard, A. W., Halverson, S., et al. 2024, *Astron. J.*, 168, 101
- Dai, F., Masuda, K., & Winn, J. N. 2018, *ApJ*, 864, L38
- Dai, F., Masuda, K., Winn, J. N., & Zeng, L. 2019, *Astrophys. J.*, 883, 79
- Dai, F., Winn, J. N., Arriagada, P., et al. 2015, *The Astrophysical Journal Letters*, 813, L9
- Deacon, N. R., Groot, P. J., Drew, J. E., et al. 2009, *Monthly Notices of the Royal Astronomical Society*, 397, 1685
- Deeg, H. J., Georgieva, I. Y., Nowak, G., et al. 2023, *Astron. Astrophys.*, 677, A12
- Demory, B.-O., Gillon, M., de Wit, J., et al. 2016, *Nature*, 532, 207
- Dotter, A. 2016, *ApJS*, 222, 8
- Espinoza, N., Kossakowski, D., & Brahm, R. 2019, *MNRAS*, 490, 2262
- Espinoza-Retamal, J. I., Brahm, R., Petrovich, C., et al. 2023a, *ApJ*, 958, L20
- Espinoza-Retamal, J. I., Stefánsson, G., Petrovich, C., et al. 2024, *Astron. J.*, 168, 185
- Espinoza-Retamal, J. I., Zhu, W., & Petrovich, C. 2023b, *AJ*, 166, 231
- Fabrycky, D. C., Lissauer, J. J., Ragozzine, D., et al. 2017, *Architecture of Kepler's multi-transiting systems. II. New investigations with twice as many candidates.*, *VizieR On-line Data Catalog: J/ApJ/790/146*. Originally published in: 2014ApJ...790..146F
- Foreman-Mackey, D., Agol, E., Angus, R., & Ambikasaran, S. 2017, *ArXiv*
- Foreman-Mackey, D., Hogg, D. W., Lang, D., & Goodman, J. 2013, *PASP*, 125, 306
- Fulton, B. J., Petigura, E. A., Blunt, S., & Sinukoff, E. 2018, *Publ. Astron. Soc. Pac.*, 130, 044504
- Gaia Collaboration, Brown, A. G. A., Vallenari, A., et al. 2018, *A&A*, 616, A1
- Gaia Collaboration, Brown, A. G. A., Vallenari, A., et al. 2016, *A&A*, 595, A2
- Gaia Collaboration, Vallenari, A., Brown, A. G. A., et al. 2023, *Astron. Astrophys.*, 674, A1
- Goldreich, P. & Soter, S. 1966, *Icarus*, 5, 375
- Goyal, A. V. & Wang, S. 2025, *AJ*, 169, 191
- Guerrero, N. M., Seager, S., Huang, C. X., et al. 2021, *ApJS*, 254, 39
- Han, T. & Brandt, T. D. 2023, *The Astronomical Journal*, 165, 71
- Hatzes, A. P. 2014, *Astronomy & Astrophysics*, 568, A84
- Hatzes, A. P., Dvorak, R., Wuchterl, G., et al. 2010, *Astron. Astrophys.*, 520, A93
- Hill, G. J., Lee, H., MacQueen, P. J., et al. 2021, *Astron. J.*, 162, 298
- Høg, E., Fabricius, C., Makarov, V. V., et al. 2000, *A&A*, 355, L27
- Hu, R., Ehlmann, B. L., & Seager, S. 2012, *ApJ*, 752, 7
- Husser, T.-O., von Berg, S. W., Dreizler, S., et al. 2013, *Astronomy & Astrophysics*, 553, A6
- Isaacson, H. & Fischer, D. 2010, *ApJ*, 725, 875
- Jackson, B., Stark, C. C., Adams, E. R., Chambers, J., & Deming, D. 2013, *ApJ*, 779, 165
- Jenkins, J. M., Twicken, J. D., McCauliff, S., et al. 2016, in *Society of Photo-Optical Instrumentation Engineers (SPIE) Conference Series*, Vol. 9913, Software and Cyberinfrastructure for Astronomy IV, ed. G. Chiozzi & J. C. Guzman, 99133E
- Jones, S. E., Stefánsson, G., Masuda, K., et al. 2024, *AJ*, 168, 93
- Kaplan, K. F., Bender, C. F., Terrien, R. C., et al. 2019, in *Astronomical Society of the Pacific Conference Series*, Vol. 523, *Astronomical Data Analysis Software and Systems XXVII*, ed. P. J. Teuben, M. W. Pound, B. A. Thomas, & E. M. Warner, 567
- Kempton, E. M.-R., Bean, J. L., Louie, D. R., et al. 2018, *Publications of the Astronomical Society of the Pacific*, 130, 114401
- Königl, A., Giacalone, S., & Matsakos, T. 2017, *ApJ*, 846, L13
- Kreidberg, L. 2015, *Publ. Astron. Soc. Pac.*, 127, 1161
- Kreidberg, L., Koll, D. D. B., Morley, C., et al. 2019, *Nature*, 573, 87
- Kurucz, R. 1993, *ATLAS9 Stellar Atmosphere Programs and 2 km/s grid*. Kurucz CD-ROM No. 13. Cambridge, 13
- Lam, K. W. F., Csizmadia, S., Astudillo-Defru, N., et al. 2021, *Science*, 374, 1271
- Lee, E. J. & Chiang, E. 2017, *Astrophys. J.*, 842, 40
- Lee, R. A., Dai, F., Howard, A. W., et al. 2025, *ApJ*, 983, L36
- Lightkurve Collaboration, Cardoso, J. V. d. M., Hedges, C., et al. 2018, *Lightkurve: Kepler and TESS time series analysis in Python*, *Astrophysics Source Code Library*
- Lopez, E. D. 2017, *MNRAS*, 472, 245
- Luhn, J. K., Wright, J. T., Howard, A. W., & Isaacson, H. 2020, *AJ*, 159, 235
- Lundkvist, M. S., Kjeldsen, H., Albrecht, S., et al. 2016, *Nature Communications*, 7, 11201
- Mahadevan, S., Ramsey, L., Bender, C., et al. 2012, in *Ground-based and Airborne Instrumentation for Astronomy IV*, ed. I. S. McLean, S. K. Ramsay, & H. Takami (SPIE)
- Marcus, R. A., Sasselov, D., Hernquist, L., & Stewart, S. T. 2010, *ApJ*, 712, L73
- Masci, F. J., Laher, R. R., Rusholme, B., et al. 2019, *PASP*, 131, 018003
- Mazeh, T., Holczer, T., & Faigler, S. 2016, *A&A*, 589, A75
- Metcalf, A. J., Anderson, T., Bender, C. F., et al. 2019, *Optica*, 6, 233
- Millholland, S. C. & Spalding, C. 2020, *ApJ*, 905, 71
- Munari, U., Henden, A., Frigo, A., et al. 2014, *AJ*, 148, 81
- Murgas, F., Nowak, G., Masseron, T., et al. 2022, *Astron. Astrophys.*, 668, A158
- Ninan, J. P., Bender, C. F., Mahadevan, S., et al. 2018, in *High Energy, Optical, and Infrared Detectors for Astronomy VIII*, ed. A. D. Holland & J. Beletic, Vol. 10709, *International Society for Optics and Photonics (SPIE)*, 107092U
- Pecaut, M. J. & Mamajek, E. E. 2013, *ApJS*, 208, 9
- Penev, K., Bouma, L. G., Winn, J. N., & Hartman, J. D. 2018, *AJ*, 155, 165
- Perryman, M., Hartman, J., Bakos, G. Á., & Lindegren, L. 2014, *ApJ*, 797, 14
- Perryman, M. A. C., Lindegren, L., Kovalevsky, J., et al. 1997, *A&A*, 323, L49
- Petrovich, C., Deibert, E., & Wu, Y. 2019, *AJ*, 157, 180
- Price, E. M. & Rogers, L. A. 2020, *Astrophys. J.*, 894, 8
- Pu, B. & Lai, D. 2019, *MNRAS*, 488, 3568
- Ramsey, L. W., Weedman, D. W., Ray, F. B., & Sneden, C. 1988, in *European Southern Observatory Conference and Workshop Proceedings*, Vol. 30, *Very Large Telescopes and their Instrumentation*, Vol. 2, ed. M. H. Ulrich, 119
- Rappaport, S., Sanchis-Ojeda, R., Rogers, L. A., Levine, A., & Winn, J. N. 2013, *Astrophys. J. Lett.*, 773, L15
- Ricker, G. R., Winn, J. N., Vanderspek, R., et al. 2014, *Journal of Astronomical Telescopes, Instruments, and Systems*, 1, 014003
- Sahu, K. C., Casertano, S., Bond, H. E., et al. 2006, *Nature*, 443, 534
- Sanchis-Ojeda, R., Rappaport, S., Winn, J. N., et al. 2014, *Astrophys. J.*, 787, 47
- Schlaufman, K. C., Lin, D. N. C., & Ida, S. 2010, *ApJ*, 724, L53
- Schwab, C., Rakich, A., Gong, Q., et al. 2016, in *Society of Photo-Optical Instrumentation Engineers (SPIE) Conference Series*, Vol. 9908, *Ground-based and Airborne Instrumentation for Astronomy VI*, ed. C. J. Evans, L. Simard, & H. Takami, 99087H
- Scott, N. J., Howell, S. B., Horch, E. P., & Everett, M. E. 2018, *Publ. Astron. Soc. Pac.*, 130, 054502
- Silvotti, R., Charpinet, S., Green, E., et al. 2014, *Astron. Astrophys.*, 570, A130
- Skrutskie, M. F., Cutri, R. M., Stiening, R., et al. 2006, *AJ*, 131, 1163
- Smith, A. M. S., Cabrera, J., Csizmadia, S., et al. 2018, *Mon. Not. R. Astron. Soc.*, 474, 5523
- Speagle, J. S. 2020, *MNRAS*, 493, 3132
- Stassun, K. G., Oelkers, R. J., Paegert, M., et al. 2019, *AJ*, 158, 138
- Stassun, K. G., Oelkers, R. J., Pepper, J., et al. 2018, *AJ*, 156, 102
- Stefansson, G., Cañas, C., Wisniewski, J., et al. 2020, *The Astronomical Journal*, 159, 100
- Stefánsson, G., Mahadevan, S., Miguel, Y., et al. 2023, *Science*, 382, 1031
- Stefánsson, G., Mahadevan, S., Petrovich, C., et al. 2022, *Astrophys. J. Lett.*, 931, L15
- Steffen, J. H. & Farr, W. M. 2013, *ApJ*, 774, L12
- Tu, P.-W., Xie, J.-W., Chen, D.-C., & Zhou, J.-L. 2025, *Nature Astronomy* [arXiv:2504.20986]
- Uzsoy, A. S. M., Rogers, L. A., & Price, E. M. 2021, *Astrophys. J.*, 919, 26
- Valsecchi, F., Rappaport, S., Rasio, F. A., Marchant, P., & Rogers, L. A. 2015, *ApJ*, 813, 101
- Vanderspek, R., Huang, C. X., Vanderburg, A., et al. 2019, *ApJ*, 871, L24
- Vines, J. I. & Jenkins, J. S. 2022, *MNRAS* [arXiv:2204.03769]
- Vleeschower, L., Corongiu, A., Stappers, B. W., et al. 2024, *Mon. Not. R. Astron. Soc.*, 530, 1436
- Whittaker, E. A., Malik, M., Ih, J., et al. 2022, *AJ*, 164, 258
- Wilkins, A. N., Delrez, L., Barker, A. J., et al. 2017, *ApJ*, 836, L24
- Winn, J. N., Sanchis-Ojeda, R., & Rappaport, S. 2018, *New Astronomy Reviews*, 83, 37
- Winn, J. N., Sanchis-Ojeda, R., Rogers, L., et al. 2017, *AJ*, 154, 60
- Wright, E. L., Eisenhardt, P. R. M., Mainzer, A. K., et al. 2010, *AJ*, 140, 1868
- Wright, J. T. 2005, *PASP*, 117, 657
- Zechmeister, M., Reiners, A., Amado, P. J., et al. 2018, *Astron. Astrophys.*, 609, A12
- Zeng, L., Jacobsen, S. B., Sasselov, D. D., et al. 2019, *Proceedings of the National Academy of Sciences*, 116, 9723
- Zhang, M., Hu, R., Inglis, J., et al. 2024, *ApJ*, 961, L44
- Zilinskas, M., van Buchem, C. P. A., Miguel, Y., et al. 2022, *A&A*, 661, A126

Appendix A: Radial Velocities

Table A.1 lists the RVs of TOI-2431.

Table A.1. RVs of TOI-2431. The median S/N for NEID observations is 27 at 860 nm, and the median S/N of the HPF observations is 205 at $1\ \mu\text{m}$. The RVs used in the FCO fit—the nights that had two or more observations obtained within a night—are denoted with "Y" in the FCO column. All of the RVs were used for the GP joint fit.

Time (BJD _{TDB})	Radial Velocity (m s^{-1})	Instrument	FCO
2460661.694342	-9.0 ± 2.6	NEID	Y
2460661.834318	-21.9 ± 3.1	NEID	Y
2460663.818467	-1.9 ± 2.4	NEID	N
2460664.634615	6.4 ± 1.8	NEID	N
2460665.583873	9.8 ± 1.8	NEID	N
2460680.644771	-12.1 ± 4.2	NEID	Y
2460680.746552	6.8 ± 2.8	NEID	Y
2460685.702258	4.6 ± 5.8	NEID	N
2460725.617289	-1.4 ± 3.0	NEID	Y
2460725.621031	-6.3 ± 2.7	NEID	Y
2460725.672322	-16.3 ± 5.6	NEID	Y
2460725.675878	-11.3 ± 5.4	NEID	Y
2460673.709907	-25.2 ± 10	HPF	N
2460712.606630	13.3 ± 7.3	HPF	N
2460715.597665	5.9 ± 5.0	HPF	N

Figure B.1 also highlights the recovered semi-amplitudes as a function injected RV semi-amplitudes. This shows that there is no bias introduced in the recovered RV semi-amplitudes of the synthetic planet b at the RV amplitude of TOI-2431 b of $8.3\ \text{m s}^{-1}$. From this, we conclude that the FCO method, in combination with the available NEID RV observations results in a robust determination of the RV amplitude of TOI-2431 b.

Appendix B: Injection and Recovery Tests for the FCO Method

To assess the robustness of the Floating Chunk Offset (FCO) method for our joint fitting of the NEID and TESS data in the limit where we had 8 observations spread over 3 NEID visits, we carried out a series of injection and recovery tests.

For the injection and recovery tests, we created a series of synthetic RV datastreams evaluated at the same NEID timestamps as used in the adopted fit in Section 4 and listed in Table A.1. The RV uncertainties were assumed to be the same RV uncertainties as the as-observed uncertainties as listed in Table A.1. To simulate the impact of the excess RV scatter we see in the system we assumed two planets in the system: planet b, which we assumed has the same orbital period and transit midpoint as our best-fit in Table 2, and another outer planet c in the system. We assumed planet c had an orbital period P_c between 1 to 100 days. For planet c, we randomly sampled the time of periastron from $-P_c/2$ to $P_c/2$. For both planets, we assume circular orbits. We then varied the RV semi-amplitudes of both planets b and c, uniformly sampled from 0 to $50\ \text{m s}^{-1}$.

In total, we generated 1500 synthetic such RV datastreams, keeping track of the known injected parameters of planet b and planet c. We then ran these synthetic RV datastreams through our FCO fitting method to test if we accurately recover the parameters of planet b, irrespective of the parameters of the outer companion. Here we define "recovered" if the recovered semi-amplitude of planet b is within 3σ range of the injected semi-amplitude.

Figure B.1 summarizes the results of the injection and recovery tests. In Figure B.1 blue points show 'recovered' values of planet b, while red points denote cases that were not recovered: out of 1500 injections, we have recovered the semi-amplitude from 1498 of them, suggesting a 99.87% recovery rate. This frequency corresponds to the $3\sigma \sim 99.7\%$ definition of recovered from the total population.

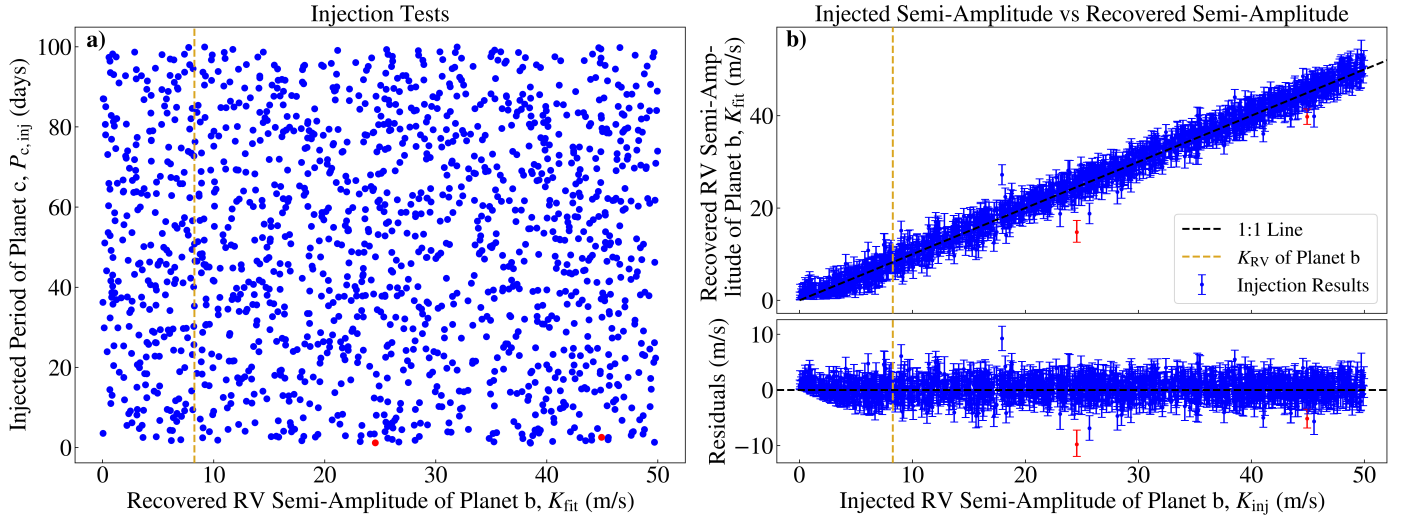


Fig. B.1. Summary of injection and recovery test to test the robustness of the FCO method in the limit of 8 NEID observations obtained in 3 different visits. **a)** Injected semi-amplitudes of a hypothetical planet c as a function of the injected RV amplitude of the assumed planet b. Blue dots represent runs where the RV amplitude of planet b was successfully recovered (within 3σ of the injected value), while the red dots indicate non-recovered runs. The semi-amplitude of TOI-2431 b from Table 2 is highlighted with the yellow vertical line. **b) Top:** Recovered RV semi-amplitudes K_{fit} as a function of injected RV semi-amplitudes for planet b. Similar to a), blue dots represent recovered runs, whereas red dots indicate non-recovered runs, and the yellow vertical line indicates our adopted RV semi-amplitude of TOI-2431 b from Table 2. The 1-1 line is indicated with the black dashed line. We see that the recovered values are in good agreement with the injected values.